Earth and Planetary Science Letters 567 (2021) 117000

Contents lists available at ScienceDirect

Earth and Planetary Science Letters

www.elsevier.com/locate/epsl

Mica kink-band geometry as an indicator of coseismic dynamic loading

Erik K. Anderson *, Won Joon Song, Scott E. Johnson, Alicia M. Cruz-Uribe

School of Earth and Climate Sciences, University of Maine, Orono, ME 04469, USA

ARTICLE INFO

Article history:
Received 9 October 2020
Received in revised form 4 May 2021
Accepted 7 May 2021
Available online xxxx
Editor: R. Bendick

Keywords:
kink band
paleoseismicity
frictional-to-viscous transition
earthquake source
dynamic loading
mica

ABSTRACT

Recognizing that exhumed shear zones had a seismogenic history is an important prerequisite for microstructural studies of energy partitioning in the earthquake source region. Using optical measurements of kinked micas along the Sandhill Corner shear zone, a seismogenic fault/shear zone exhumed from the base of the frictional-to-viscous transition, we demonstrate that their geometric properties are statistically different from kinks in micas that underwent regional deformation and metamorphism. Kink-band asymmetries and the angles of external rotation are larger in rocks from the Sandhill Corner shear zone, whereas kink-band widths are smaller. Our data show remarkable similarities to kink bands from dynamic deformation experiments, meteorite impacts, and nuclear explosion sites, suggesting a dynamic origin for their formation. Our results suggest that mica kink bands may be a useful indicator of dynamic loading and paleoseismicity in the rock record.

1. Introduction

Earthquakes associated with fault slip represent the release of elastic strain energy accumulated during interseismic loading. Although radiated seismic waves are the most readily measured component of the earthquake energy budget, most of the energy associated with rupture propagation is dissipated in the source region as frictional heat (e.g., Pittarello et al., 2008) and a variety of inelastic processes such as microcracking (e.g., Chester et al., 2005). Direct structural and microstructural observations in the source volume of exhumed fault zones are therefore necessary to better quantify the earthquake energy budget. As such, it is important to identify exhumed fault zones that sustained coseismic damage.

Up until the 21st century, definitive evidence for paleoseismicity in the rock record was restricted to pseudotachylyte (Cowan, 1999 and references therein), which is widely interpreted to result from coseismic frictional melting. Since then, field-based observations in active and exhumed seismogenic faults have revealed further evidence related to characteristic features of earthquakes, such as high fault slip rates and rupture propagation velocities (Rowe and Griffith, 2015 and references therein). These features include byproducts of frictional devolatilization, maturation of organic material, mobilization of trace elements, injection of veins, and pulverization of rocks. As many of these features can become erased at greater depths in faults and shear zones due to viscous overprinting, additional criteria would be useful to recognize paleoseismicity along faults exhumed from the deeper reaches of the seismogenic zone.

Following the advent of nuclear explosives in the mid-1900s, interest was sparked in their use in land development and achieving a better understanding of terrestrial impact craters (Short, 1965). As part of this work, scientists needed to characterize how shock waves emanating from the explosions affected the mechanical and microstructural properties of the surrounding rock. Observed changes in mechanical and physical properties included variations in fracture density, porosity, crushing strength, mass density, Young's modulus, and sonic velocity. These changes were accompanied microstructurally by the occurrence of Mode I and II microcracks in quartz and feldspar, deformation lamellae in quartz, and kink bands in micas. Because kink bands had been used to understand the stress conditions for rocks undergoing quasi-static loading (Dewey, 1965), it was postulated that they could be used to indicate the magnitude and direction of stress waves following dynamic loading events (Short, 1965, 1966).

This prompted several studies in the 1960s to characterize the geometry of kink bands in micas from various tectonic settings (Fig. 1). From this work came the observation that the degree of asymmetry ($\delta - \varepsilon$), kink-band width (d), and the angle of external rotation (ω) in micas showed statistically distinct zones representative of quasi-static versus dynamic loading conditions (Borg and Handin, 1966; Hörz and Ahrens, 1969; Hörz, 1970). Samples deformed under quasi-static conditions were intended to approximate kink-band formation under natural conditions of re-

* Corresponding author.
E-mail addresses: erik.k.anderson@maine.edu (E.K. Anderson), wonjoon.song@maine.edu (W.J. Song), johnsons@maine.edu (S.E. Johnson), alicia.cruzuribe@maine.edu (A.M. Cruz-Uribe).

https://doi.org/10.1016/j.epsl.2021.117000
0012-821X/

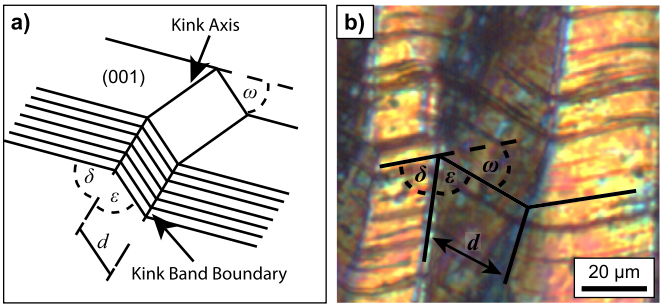

Fig. 1. Kink-band geometry and measurement. a) Geometric features of kinked micas in three dimensions. δ and ε - kink angles. ω - angle of external rotation. d - kink width. $\delta + \varepsilon + \omega = 180°$. b) Photomicrograph (cross-polarized light) of a part of a kinked mica from the Sandhill Corner shear zone, illustrating the location of measured geometric features. See Fig. 3c for the entire muscovite grain. (For interpretation of the colors in the figure(s), the reader is referred to the web version of this article.)

gional deformation, whereas those deformed under dynamic conditions were intended to approximate kink-band formation associated with meteorite impacts (e.g., Stöffler, 1966) and nuclear explosions (Short, 1966). Quasi-static deformation experiments also explored the influence of kinematics in their formation under both axial compression (Borg and Handin, 1966; Patterson and Weiss, 1966; Etheridge et al., 1973) and torsion (Misra and Burg, 2012).

In the present paper, we show that the geometry of kink bands in mica grains within an exhumed, seismogenic fault/shear zone exhibit features that are markedly different from micas deformed under conditions of regional deformation and metamorphism. These observations suggest that kink bands can potentially be used as an indicator of dynamic loading and paleoseismicity in the rock record.

2. Geologic background

Samples used in this study come from two locations in the state of Maine, USA that underwent different deformation histories: 1) the paleoseismogenic Sandhill Corner shear zone of the Norumbega fault system, and 2) the low-pressure, high-temperature regional metamorphic rocks of western Maine. A summary of the geologic context of the samples and their relationship to inferred loading rates is provided below (Fig. 2).

2.1. Sandhill Corner shear zone

During the Acadian orogeny in south-central Maine, the regional style of deformation shifted from contraction to dextral transpression, resulting in the formation of the Norumbega fault system (e.g., West and Hubbard, 1997). The Norumbega fault system is a crustal-scale, steeply-dipping, large-displacement, dextral transcurrent fault characterized by two styles of deformation. The first manifests itself in a 30–40 km wide zone of dextral shear that initiated at ~380 Ma (Gerbi and West, 2007). This event is characterized by the development of open, northerly-trending, asymmetric z-folds with steeply dipping axial planes and shallow- to moderately plunging fold axes (e.g., West et al., 2003). Overprinting this wide zone of dextral shear are several relatively narrow (0.1–1.5 km wide) zones of mylonitization (e.g., Ludman and West, 1999; Price et al., 2016). Whereas widespread deformation along the Norumbega fault system initiated during the Acadian orogeny and lasted for ~20 Myr, localized strain along the mylonite zones shows activity spanning 100 Myr with two periods of reactivation occurring during the late Paleozoic and Mesozoic (e.g., West and Hubbard, 1997). Among the longest continuous mylonite zones in the Norumbega fault system is the Sandhill Corner shear zone (SCSZ), a seismogenic fault exhumed from the base of the frictional-to-viscous transition zone (Fig. 2b; Price et al., 2012, 2016). The rocks in this area underwent dynamic loading as evidenced by the occurrence of pseudotachylyte (Price et al., 2012), particle size distributions of garnet fragments (B.R. Song et al., 2020), and abundance of fluid-inclusions along healed microcracks (W.J. Song et al., 2020).

2.2. Western Maine

The rocks from western Maine (WM) are part of the Perry Mountain Formation, a Silurian-aged turbidite sequence located in the Central Maine Belt (Fig. 2c; Johnson et al., 2006). These rocks are polymetamorphic and polydeformed, preserving two major deformation events. The first involved the development of upright, northeast-trending, tight, isoclinal folds associated with a period of regional contraction during the Siluro-Devonian Acadian orogeny at ~400 Ma (e.g., Moench, 1970; Smith and Barreiro, 1990). Overprinting this regional fold pattern, local crenulation cleavage developed in response to the intrusion of plutons, such as the Mooselookmeguntic pluton, ~20–30 Myr later (Johnson et al., 2006). Our samples were chosen to avoid these localized overprinting deformation events. No evidence of paleoseismicity is apparent in the rocks of WM.

3. Methods

The geometry of kink bands (δ, ε, and d in Fig. 1) was measured using the rotating stage on a polarized light microscope. The two kink angles (δ and ε) were recorded as $\delta > \varepsilon$, so that the kink-band asymmetry ($\delta - \varepsilon$) is always $\geq 0°$. The angle of external rotation (ω) was calculated by subtracting the sum of δ and ε from 180°. Only kink bands where slip associated with kinking occurred on one side of the band were measured (i.e., primary kink bands of Etheridge et al., 1973). To provide statistically meaningful data, as many distinct kink bands as possible within a given grain were measured per sample (~45–58 kink bands). We investigated 124 muscovite and biotite grains in eight thin sections (in the XZ plane; Fig. 3a) from the SCSZ and 84 biotite grains in three thin sections (in the YZ plane; Fig. 4a) from WM.

Because these measurements are sensitive to the orientation of the thin section relative to the kink axis, care was taken to ensure that the angles measured were true and not apparent. In the SCSZ, the kinematic reference frame is well-defined based on field observations (Figs. 2b and 3b) and a calculated kinematic vorticity number of 0.97 (Johnson et al., 2009). In contrast, rocks from WM are more ambiguous. Three orthogonal sections were cut from WM rocks to identify the appropriate plane for measurement. Electron backscatter diffraction (EBSD) measurements of biotite were also made on polished thin sections to confirm that our chosen section represents the appropriate reference frame for optical kink-band measurements. The thin section was coated with a thin layer of carbon to prevent electrical charging. EBSD data were collected using a Tescan Vega II Scanning Electron Microscope equipped with an EDAX-TSL EBSD system at the University of Maine. EDAX-TSL OIM Data Collection 5.31 software was used to acquire diffraction patterns using an acceleration voltage of 20 kV, a beam current of ~6 nA, 70° sample tilt, and high-vacuum conditions with a square grid at 2 μm step size. Raw indexing rates of biotite were >99%. Post-processing of biotite based on confidence index (CI) and neighboring orientations was conducted using EDAX-TSL OIM Analysis 5.31 software. Non- and poor-indexed pixels (CI < 0.02) were replaced with well-indexed neighbors (CI ≥ 0.02). The well-indexed pixels of biotite were ~56% of analyzed pixels. Grains in post-processing are defined by an internal misorientation <10° and a minimum grain size of 45 pixels, equivalent to ~15 μm in

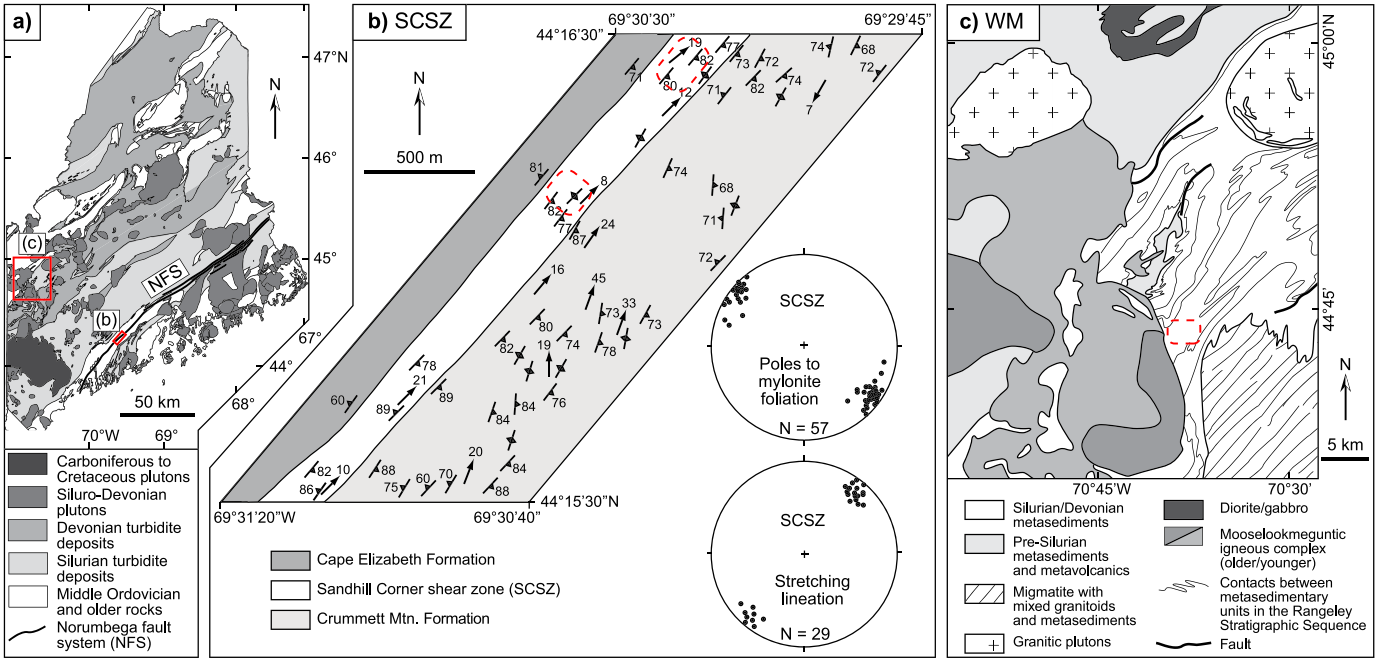

Fig. 2. Geologic maps of the study areas. a) Generalized geologic map of the state of Maine, USA showing the locations of two field areas (red boxes). Modified after Bradley et al. (2000). b) Geologic map of the Sandhill Corner shear zone (SCSZ) in the Norumbega fault system. Kinked mica grains in the SCSZ were sampled from the mylonitic portion of the shear zone (red dashed boxes). Geology and orientation data of foliation and lineation are after Grover and Fernandes (2003) and West and Peterman (2004). c) Geologic map of western Maine (WM). Measured biotite grains in WM were sampled from the Perry Mountain Formation located within the Silurian/Devonian metasediments (red dashed box). Modified after Johnson et al. (2011).

diameter. Mis-indexed biotite pixels were corrected using a pseudosymmetry cleanup routine, by comparing EBSD maps and photomicrographs. To display the crystallographic orientation of each pixel in biotite, we first generated inverse pole figure (IPF) maps aligned with two geographic directions: (1) the normal direction (X) to the thin section, and (2) one horizontal direction (Y) within the thin section indicated in the included reference frame (Fig. 5). The colors in the IPF maps correspond to the specified sample (geographic) direction with respect to crystallographic axes within the map area. A color key (semicircle for monoclinic biotite) for the IPF maps provides crystallographic reference. Next, we generated IPFs showing the two sample directions relative to the crystal reference frame and a pole figure showing c-axes relative to the sample reference frame. The IPFs and pole figure are plotted as an equal area projection with contour intensity calculated by a series expansion of generalized spherical harmonics using smoothing parameters with series rank of 10 and Gaussian half-width of 10°. An image quality (related to the quality of a diffraction pattern) map of biotite is included (Fig. 5) to visualize kink bands since it reproduces surface damage and misorientation boundaries.

4. Results

4.1. Orientation of kinked micas

Fig. 3 shows the orientation of micas with respect to the kinematic reference frame of the SCSZ. In the SCSZ, kink axes are clearly visible in the field on muscovite (001) planes exposed on foliation surfaces (Fig. 3b). These kink-band axes are oriented perpendicular to the mineral lineation defined by aligned mica grains. Because of these observations and the high-strain nature of the shear zone, we are confident that kink bands measured in sections cut in the XZ plane (Fig. 3c) closely approximate true and not apparent angles.

In the WM rocks, three orthogonal sections were cut to investigate the orientations of the kink bands relative to the kinematic reference frame (Fig. 4). From these sections, no kink bands are visible in the XY sections (Fig. 4b). The traces of kink axes are visible in XZ sections and lie within the foliation plane parallel to the lineation (Fig. 4c), and kink bands are well-developed in YZ sections (Fig. 4d). To confirm that the YZ section in WM rocks is the profile plane for the kink bands, EBSD measurements were collected on a kinked biotite grain to verify that the (001) planes of the biotite grain lie perpendicular to the YZ plane (Fig. 5). The IPF map and IPF of the kinked biotite aligned with the normal direction to the thin section (X-direction) show that the X-direction is concentrated between either (−100) and [010] or (100) and [010] within the a-b plane of biotite (Figs. 5c and 5e). In complementary contrast, the IPF map and IPF of the biotite grain aligned with the horizontal direction within the thin section (Y-direction) show that the Y-direction is clustered near the c-axis, or [001], of biotite (Figs. 5d and 5f). The biotite pole figure shows c-axis concentrations on the primitive circle with maxima subparallel to the Y-axis (Fig. 5g). The combination of observations from the IPFs and pole figure indicate that the kink-band angles in the WM rocks were measured in a plane that closely approximates the kink-band profile plane.

4.2. Kink-band angles and widths

Four geometrical measurements of kink bands (Table S1) are shown in Fig. 6: δ versus ε, distribution of ω, cumulative distribution of $\delta - \varepsilon$, and cumulative distribution of d. Data and trendlines from Borg and Handin (1966), Hörz and Ahrens (1969), Hörz (1970), Etheridge et al. (1973), and Misra and Burg (2012) are overlaid for reference. These authors are hereafter referred to as BH66, HA69, H70, E73, and MB12, respectively. BH66 and HA69 reported ranges of δ, ε, and d in quasi-statically deformed and shock experiments, respectively, of biotite single crystals. H70 provided average cumulative curves of $\delta - \varepsilon$ and d for shock experiments performed on single-crystal biotite and regional metamorphosed schist containing kinked biotite and/or muscovite grains. Individual

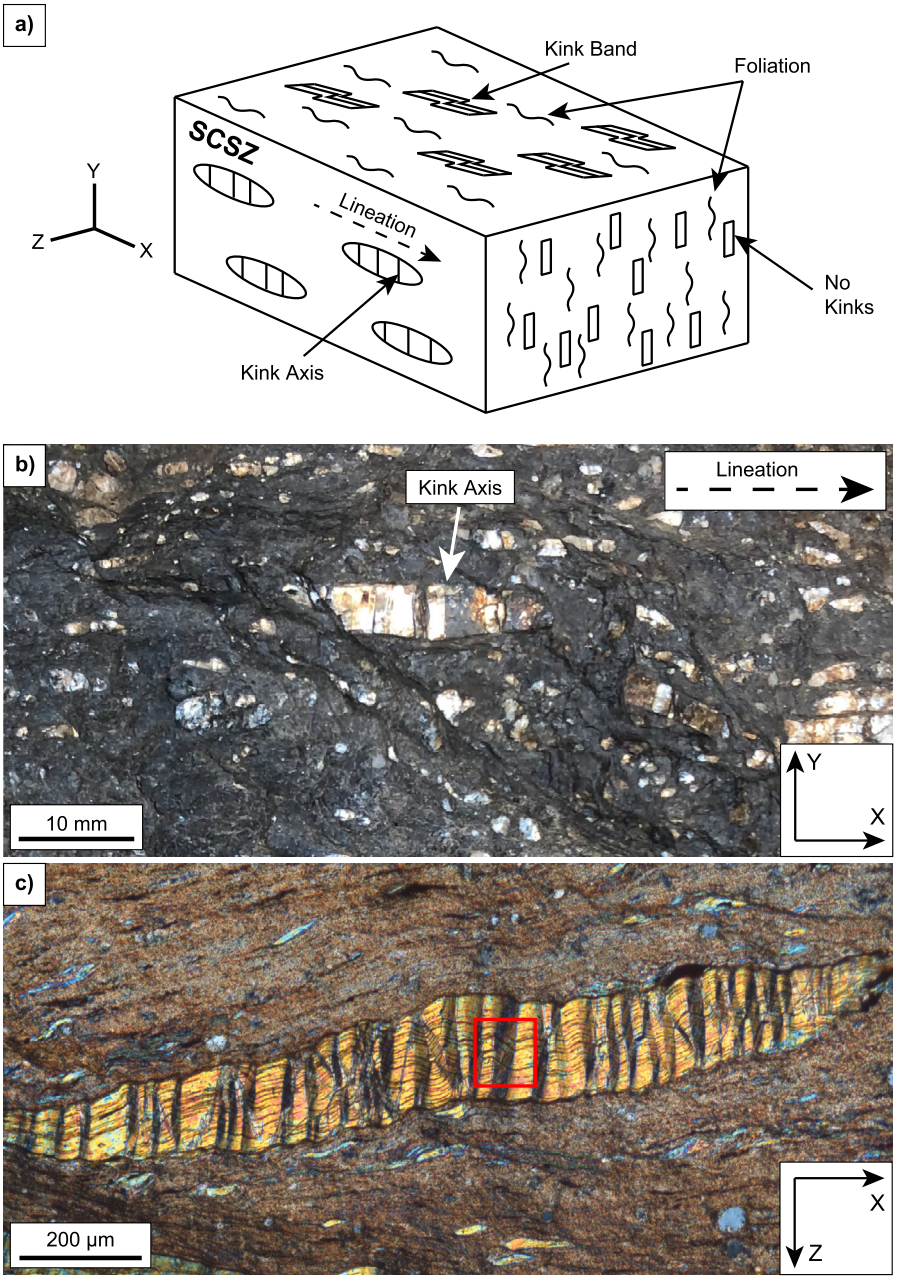

Fig. 3. Sandhill Corner shear zone (SCSZ) kinked micas. a) Schematic diagram showing the three-dimensional distribution of kink-band features in the SCSZ. b) Hand sample photo demonstrating the trace of kink axes in a muscovite grain that are clearly visible in the XY plane containing the foliation. The strong mineral lineation is also apparent in this plane. c) Photomicrograph (cross-polarized light) of muscovite kink bands in the XZ plane, perpendicular to foliation and parallel to lineation. Red box in Fig. 3c marks the location of the kink band in Fig. 1b.

data points from H70 were not available so the published average trend lines are shown for comparison. E73 provided histograms of $\delta - \varepsilon$ and ω for quasi-static, axial compression experiments performed on single crystals of biotite along directions perpendicular to the c-axis at temperatures ranging from 300–700 °C. Unless otherwise noted, we choose to compare our data to the data measured from primary kink bands in experiments performed by E73 at 300 °C, as this data set is the only one fully represented across all variables of interest. Individual data points were not recorded in E73, so comparison with our data is limited.

Fig. 6a shows a plot of δ versus ε measured from micas in the SCSZ and WM. Data are plotted on or above the one-to-one line ($\delta = \varepsilon$) as $\delta > \varepsilon$ by definition. Whereas most samples from WM plot close to the one-to-one line and within the field of quasi-statically deformed biotite in experiments by BH66, those from the SCSZ are more widely scattered and overlap with the field of shocked biotite crystals from HA69. Data from MB12 extend parallel to the field of BH66 to lower values of δ and ε at asymmetries $< \sim 10°$.

Fig. 6b shows a histogram of ω for rocks from the SCSZ, WM, and E73, with the ranges of measurements performed by BH66 and HA69 overlaid for reference. The bin size of 20° in the histogram is based on the available data from E73. Whereas kinks from micas in WM and E73 are confined to external rotation angles less than 90°, with one value of 162° being, the largest value of ω we are aware of in the literature (Borg and Handin, 1966; Hörz and Ahrens, 1969; Hörz, 1970; Etheridge et al., 1973; Misra and Burg, 2012). Most data in the quasi-static experiments of BH66 form a narrow ω range of 40–60°, whereas the shock experiments of HA69 show a wider ω range, extending to values greater than

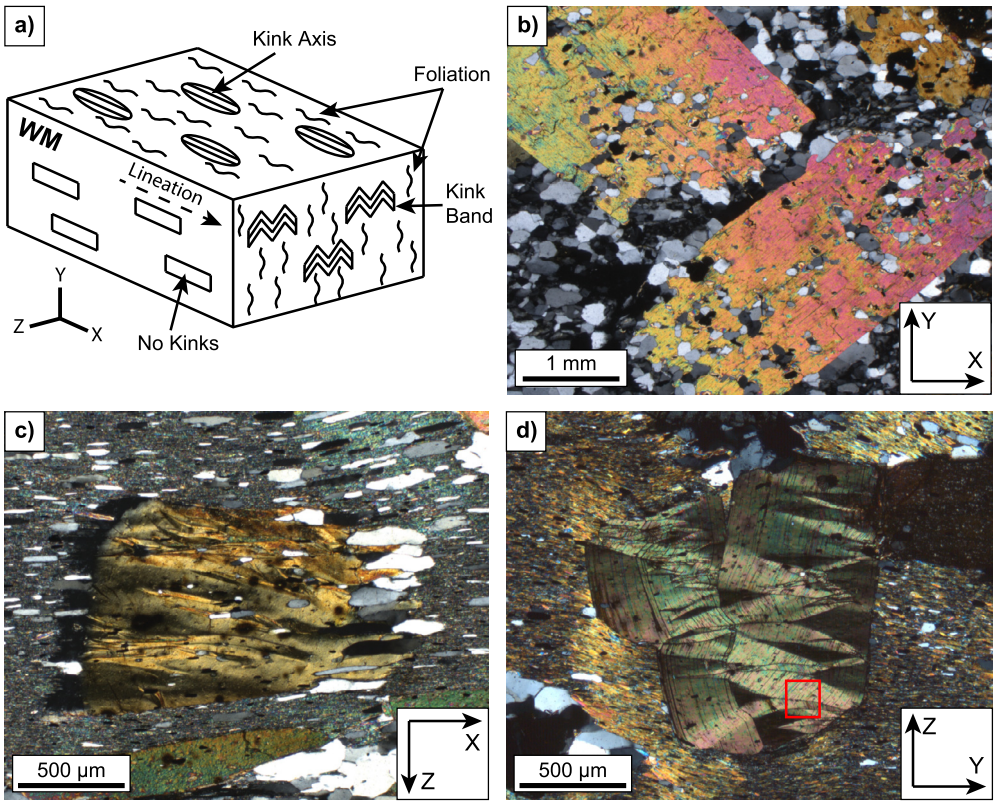

Fig. 4. Western Maine (WM) kinked micas. a) Schematic diagram showing the three-dimensional features of kink bands in WM. b) Photomicrograph (cross-polarized light) of biotite in the XY plane demonstrating the lack of observable kink bands. c) Photomicrograph (cross-polarized light) of biotite in the XZ plane showing kink axes aligned parallel to the foliation. d) Photomicrograph (cross-polarized light) of biotite in the YZ plane within which kink bands are best observed. Red box indicates the location of Fig. 9b.

90° (overturned kinks). Although H70 noted that ~10% of overturned kinks in the HA69 experiments might have resulted from the experimental setup, there is a clear difference in ω between the SCSZ and WM natural rock data (Fig. 6b).

Mica kink-band asymmetry ($\delta - \varepsilon$) data for each sample of the SCSZ (blue circles) and WM (orange triangles) are plotted as a cumulative frequency distribution with 1° bin interval in Fig. 6c. Two trend lines (blue and orange) of the average cumulative frequency for all data from the SCSZ and WM, respectively, are also drawn to compare with H70. The samples from the SCSZ show more asymmetric kinks than those from WM and the H70 average trend compiled from shock experiments. The kinks in the SCSZ reach a maximum asymmetry of ~40°, whereas the average from H70 shock experiments exhibit a maximum of ~25°. In contrast, the kinks from WM only reach a maximum asymmetry of ~13°, which is close to the average trend line maximum of ~10° for H70 regional deformation.

Fig. 6d shows mica kink-band width data from the SCSZ and WM plotted in the same manner as Fig. 6c using 1 μm bin intervals. A marked similarity exists in the overlap of the average kink-band width from the SCSZ rocks and those from shock experiments. The width of kink bands from the SCSZ and H70 shock experiments are relatively small with maximum values of 75–100 μm. In contrast, the rocks from WM and the averages from H70 regional metamorphism have relatively large kink-band widths with maximum values >200 μm. Although data on kink-band widths were not presented in E73, images of their low-temperature experiments yield kink bands with an average width of >100 μm (Fig. 2b of Etheridge et al., 1973), which is greater than the widest kink bands in the SCSZ.

E73 also presented histograms of kink-band asymmetry, but unlike their presentation of ω, they did not separate out primary from secondary kinks in the asymmetry histograms. Because we measured only primary kink bands in the sense of E73, we are not confident that our asymmetry data can be directly compared with theirs. With this note of caution, we display our data from the SCSZ and WM alongside those of E73 using histograms in Fig. 7. Data from quasi-statically deformed rocks of WM and E73 show asymmetries less than 30°, whereas dynamically deformed rocks of the SCSZ extend beyond 30°, up to 56°.

5. Discussion

5.1. Kinematic models of kink-band formation

The formation of kink bands was extensively studied and modeled in the 1960s, with primary interest in applications in estimating paleostress orientations and finite shortening in orogenic belts (e.g. Dewey, 1965). From these studies, four models were produced that result in variations in the kink-band angles, widths, and angles of external rotation with increasing strain (Twiss and Moores, 1992). We summarize these models below and note how the various aspects of kink-band geometry change with the goal of determining if any of them are plausible alternatives to explain our observations (see Twiss and Moores, 1992 for diagrams of the four kinematic models).

- Model I (Migrating kink-band boundary model with rotation):

The kink-band boundaries rotate and widen with increasing strain, accompanied by rotation of the internal foliation and flexural slip along the foliation (Weiss, 1980). This model results in an increase in the angle of external rotation until $\omega = 90°$ and an increase in

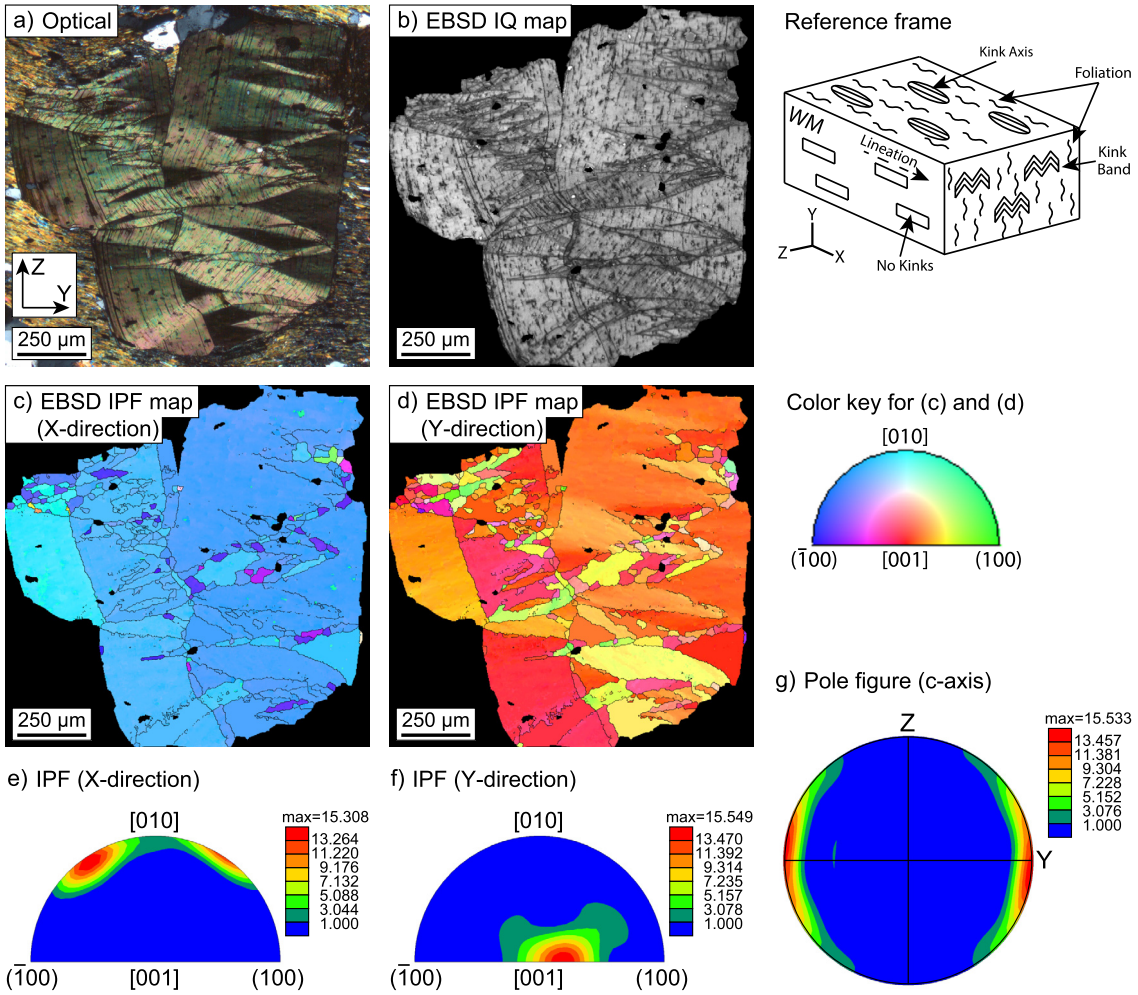

Fig. 5. Electron backscatter diffraction (EBSD) analysis of a kinked biotite grain from western Maine. a) Photomicrograph (cross-polarized light) of kinked biotite in the YZ plane (taken from Fig. 4d). The 3D reference frame (taken from Fig. 4a) is placed in the top right panel. b) Image quality (IQ) map of the biotite grain displaying kink-band boundaries by dark lines. c) EBSD inverse pole figure (IPF) map (aligned with the X-direction) of the biotite grain. The dominant bluish colors in the map indicate that the X-direction is concentrated between a- and b-axes according to the color key placed in the middle right panel (see also e). The lack of variation in blue colors indicates that we are effectively looking down the kink-band rotation axes. d) EBSD IPF map (aligned with the Y-direction) of the biotite grain. The dominant red or orange colors in the map indicate that the Y-direction is clustered around c-axes according to the color key (see also f). The variation in red-orange colors indicates that we are effectively looking perpendicular to the kink-band rotation axes. Black lines in c) and d) indicate $>10°$ misorientations between neighboring pixels. e) IPF of the kinked biotite in c), aligned with the X-direction and contoured as multiples of uniform distribution. The maxima between [010] and (-100) or (100) support the interpretation in c). f) IPF of the kinked biotite in d), aligned with the Y-direction. The maximum around [001] supports the interpretation in d). g) Lower-hemisphere c-axis pole figure of the kinked biotite grain, contoured as multiples of uniform distribution. The c-axes of all measurement points in biotite are concentrated on the primitive circle subparallel to the Y-direction, indicating that the YZ plane where kink-band angles were measured closely approximates the kink-band profile section.

kink-band width. However, the kink angles of δ and ε decrease at the same rate, resulting in symmetric kink bands.

- Model II (Migrating kink-band boundary model without rotation):

The kink-band boundary remains at constant orientation upon nucleation and grows by lateral migration through the undeformed portions of the material (Patterson and Weiss, 1966). This model results in a constant value of kink angles ($\delta = \varepsilon$) and the angle of external rotation. The kink-band width increases with increasing strain as the kink boundaries sweep into the rest of the material.

- Model III (Fixed kink-band boundary model with simple shear parallel to the boundary):

The kink band nucleates at a fixed width and maintains this constant width throughout its development. The kink-band boundary acts as a shear zone and strain is accommodated by shear parallel to the kink-band boundary, resulting in transposition of one of the limbs on top of the other and an increase in the angle of external rotation (Ramsay, 1962; Dewey, 1965). During this process, the kinks become asymmetric ($\delta \neq \varepsilon$). Since the volume inside the kink band remains constant, the length and thickness of the internal foliation within the kink band are inversely proportional to each other throughout the deformation process, initially becoming shorter and thicker and later becoming longer and thinner, respectively.

- Model IV (Fixed kink-band boundary model with rigid rotation of internal foliation):

The kink band forms by rigid rotation of the internal foliation and maintains constant length throughout the deformation process (Ramsay, 1967; Twiss and Moores, 1992). The kink-band width and degree of asymmetry ($\delta - \varepsilon$) change throughout its development. Initially, the kink band starts out asymmetric ($\delta > \varepsilon$), and as the kink develops, volume inside the kink band increases (increasing

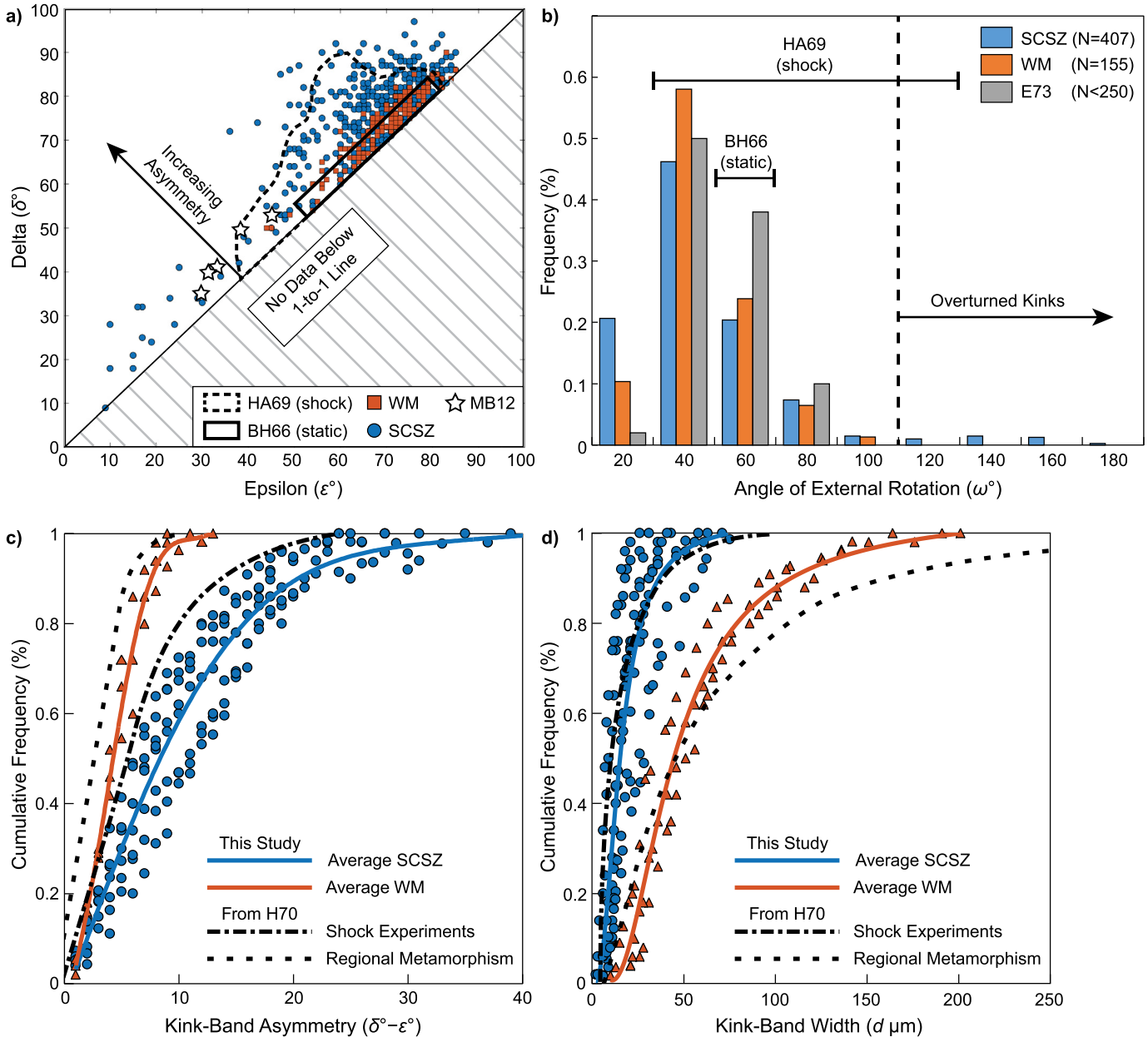

Fig. 6. Measurements of geometric features of mica kink bands from the Sandhill Corner shear zone (SCSZ) and western Maine (WM), and comparison with other studies. a) Plot of δ versus ε. Data are plotted above the $\delta = \varepsilon$ line of symmetry as $\delta > \varepsilon$. Kinks from the SCSZ are more asymmetric than those in WM, demonstrated by increased distance from the line of symmetry. b) Histogram of the angle of external rotation (ω) with bin size of 20°. Only kink bands from the SCSZ show values greater than 90° (vertical dashed line). Total number of measurements (N) is also displayed. c) Cumulative frequency distribution plot showing increased kink-band asymmetry in the SCSZ (blue circles) compared to WM (orange triangles). d) Cumulative frequency distribution plot showing decreased kink-band width in the SCSZ (blue circles) compared to WM (orange triangles). Solid blue and orange lines in c) and d) represent average trend lines. Data from Borg and Handin (1966), Hörz and Ahrens (1969), Hörz (1970), Etheridge et al. (1973), and Misra and Burg (2012) are overlaid for comparison, referred to as BH66, HA69, H70, E73, and MB12, respectively. MB12 data are displayed by stars in a), which are from torsion experiments recorded at shear strain of 3.0. E73 data are shown as gray bars in b), as E73 did not provide discrete data points for replication in other plots. N value of E73 for ω of primary kinks in b) is uncertain, although the total N for primary and secondary kinks is 250 (Etheridge et al., 1973).

d and opening gaps between the internal foliation). With further strain, the kink-band volume decreases again (decreasing d and closing the gaps between the internal foliation) and the kink band becomes more symmetric. Once the kink angles are equal ($\delta = \varepsilon$), the kink locks up and further kinking is impossible. The angle of external rotation increases progressively until $\delta = \varepsilon$.

Although these four models can explain the kink-band geometries in the regionally deformed WM rocks (relatively low ω and $\delta - \varepsilon$), none of them account for all the observed patterns of kink-band geometries in the seismogenic SCSZ rocks. The migrating kink-band boundary models (Models I and II) are characterized by symmetric kink angles ($\delta = \varepsilon$) and increasing kink-band width with increasing strain, which are not appropriate for describing the developing asymmetry and short kink-band width in the SCSZ. The fixed kink-band boundary models (Models III and IV) might approach the SCSZ observations owing to asymmetric kink bands. However, Model IV indicates $\delta \approx \varepsilon$ for high ω, which is inconsistent with the SCSZ kink bands showing high asymmetry that exceeds the maximum $\delta - \varepsilon$ ($\sim$13°) of the WM rocks even for larger ω than 90°. Additionally, in Model III, the thickness of the kink bands is held constant, which does not explain the pattern of shorter kink-band widths.

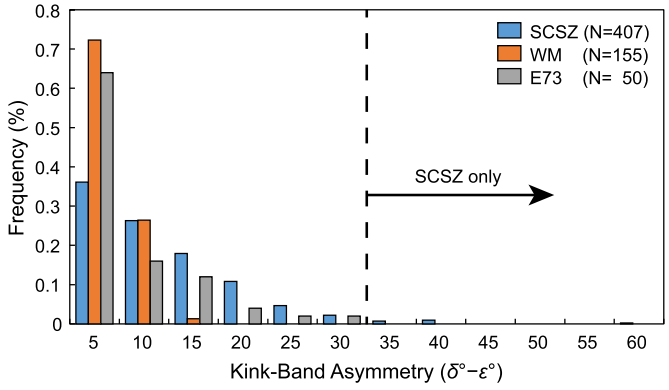

Fig. 7. Histogram of kink-band asymmetry ($\delta - \varepsilon$) with bin size of 5° for naturally- and experimentally-deformed micas. Data from the Sandhill Corner shear zone (SCSZ), western Maine (WM), and Etheridge et al. (1973; marked by E73) are shown in blue, orange, and gray, respectively. Total number of measurements (N) is also displayed. Data from quasi-statically deformed rocks of WM and E73 show asymmetries less than 30°, whereas dynamically deformed rocks of the SCSZ extend beyond 30°, up to 56°.

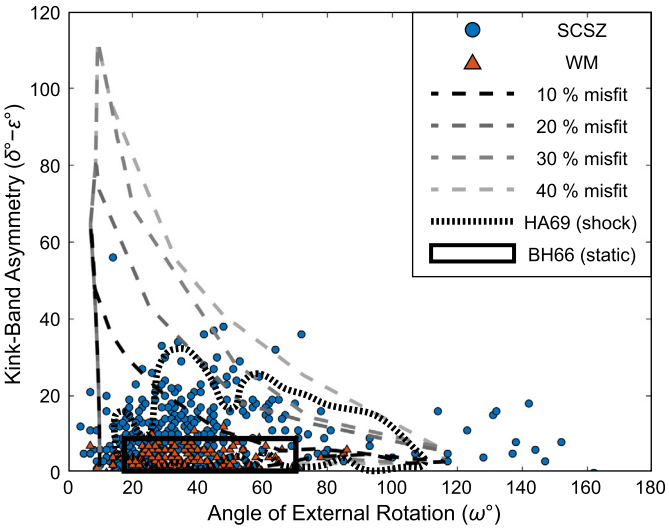

Fig. 8. Plot of kink-band asymmetry ($\delta - \varepsilon$) versus angle of external rotation (ω) for naturally- and experimentally-deformed micas. Theoretical bounds on predicted kink angles from Baronnet and Olives (1983) based on a misfit threshold are delimited by dashed curves with different shades of gray. Data from quasi-static experiments of BH66 (Borg and Handin, 1966) are outlined by the black rectangle. Maximum spreading region of shock experiments from HA69 (Hörz and Ahrens, 1969) are encircled by the finely spaced dashed curve. Data from the Sandhill Corner shear zone (SCSZ) and western Maine (WM) are shown by blue circles and orange triangles, respectively. Model input variables used are n = 1, 2, 3, and p = q = −3, −2, −1, 0, 1, 2, 3. See Baronnet and Olives (1983) for model details.

5.2. Crystallographic models of kink-band formation

The geometrical relations of kink-band angles in micas were predicted from a crystallographic model by Baronnet and Olives (1983). By minimizing the degree of lattice misfit (i.e., ≤10%) accompanying the formation of a kink band, stable equilibrium orientations were determined in $\delta - \varepsilon$ versus ω space. These orientations correspond with the kink axes [010] and <310>, as determined by observations of basal dislocation slip vectors under transmission electron microscopy (Baronnet and Olives, 1983). Fig. 8 compares our samples from the SCSZ and WM to the model of Baronnet and Olives (1983) with the experimental data of BH66 (static) and HA69 (shock) overlaid for reference. In Fig. 8, the dashed curves of varying grayscale represent boundaries containing the data predicted by their crystallographic model with varying degrees of lattice misfit (e.g., 10% to 40%).

The crystallographic model predicts discrete geometries for a given amount of allowed misfit, slip in either limb of the kink (p and q), spacing of active glide planes (n), and prescribed kink axes [010] and <310> (see Fig. 4 of Baronnet and Olives, 1983). However, similar to the fields of BH66 and HA69, considerable spread exists in the natural data from the SCSZ and WM when comparing with the predicted data of Baronnet and Olives (1983) assuming ≤10% misfit (Fig. 8). Baronnet and Olives (1983) postulated that the spread in kink-band asymmetry (e.g., the fields of BH66 and HA69) may result from either error in optical measurements, measurements of apparent versus true angles, or complex kink axes not predicted by the model. In an attempt to account for the spread in natural data, we expanded the model of Baronnet and Olives (1983) by changing the misfit up to 40% and the range of their n-values from 1–2 to 1–3 and plotted the maximum boundaries in the $\delta - \varepsilon$ versus ω space rather than discrete points. We note that the regionally deformed WM data lie almost completely within the range of BH66 for quasi-statically deformed mica (Fig. 8). The seismogenic SCSZ data show a spread comparable to HA69 for shocked mica, extending to regions well outside of the zones predicted by the crystallographic model using ≤10% misfit (Fig. 8).

Aside from the aforementioned explanations for the observed spread in natural data, we find that an alternate explanation involves increasing the misfit threshold to account for more energetically unfavorable geometries. Fig. 8 shows that most data from the SCSZ can be accounted for in this model if the misfit threshold is increased to 40%. Although some data points lay at higher values of ω than the range for 40% misfit, these can be accounted for by changing the input variables of the model (e.g., varying values of n, p, and q in Baronnet and Olives, 1983). Regardless of the input variables used, increasing amounts of misfit are required to fully account for the data in the SCSZ. Higher degrees of misfit along grain/twin/kink boundaries correspond to higher free volume, and therefore, higher surface energy (Aaron and Bolling, 1972). It has also been shown that asymmetric boundaries should have higher free volume than their symmetric counterparts (Aaron and Bolling, 1972), supporting the assertion that the kinks in the SCSZ can be explained by higher amounts of misfit.

Varying degrees of misfit could manifest themselves texturally. Backscattered electron images of micas from the SCSZ often show pronounced separation along cleavage planes associated with kinking (Fig. 9a), whereas those from WM contain little to no apparent separation along cleavage planes (Fig. 9b). The accommodation of strain associated with high misfit could manifest itself in the formation of cleavage in micas from the SCSZ. Alternatively, the folding and separation of cleavage could be related to microshear zones formed during the formation of the mylonite zone (Goodwin and Wenk, 1990). Regardless, these observations suggest that kink bands in the SCSZ are associated with higher energy microstructures compared to those in WM. We postulate that the presence of transient, dynamic stresses associated with high strain-rate loading events (i.e., earthquake rupture propagation) cause kink bands that are non-equilibrium or higher energy compared to those subjected to low strain rates, and note the similarity between the mica in Fig. 9a with the shock microstructures of HA69 and H70.

5.3. Quasi-static versus dynamic origin

The data from this study show remarkable similarity to the compiled work of BH66, HA69, H70, E73, and MB12 (Figs. 6 and 7) in that all trends for the angle of external rotation, kink-band asymmetry, and kink-band width correspond to samples with similarly interpreted geologic histories (i.e., WM experienced quasi-static stresses accompanying regional deformation and metamorphism whereas the SCSZ experienced high strain rate, dynamic

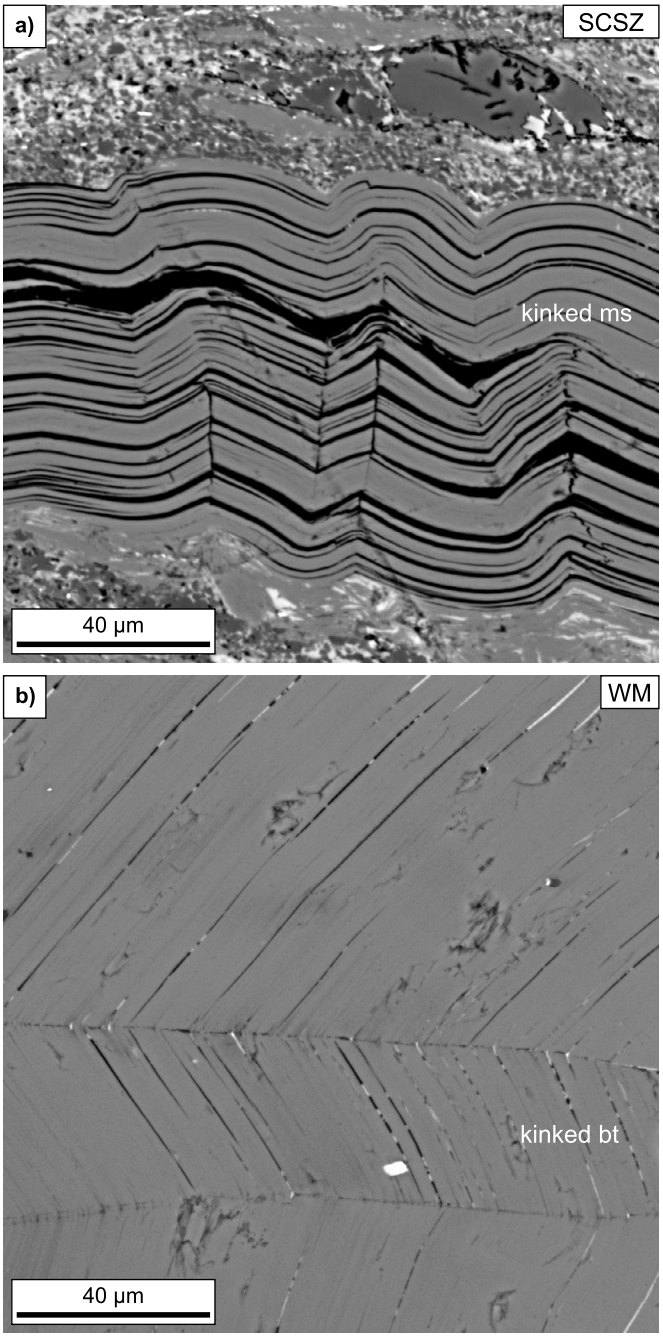

Fig. 9. Backscattered electron images of kinked micas. a) Kinked muscovite (ms) grain from the Sandhill Corner shear zone (SCSZ) showing pronounced separation of cleavage. b) Kinked biotite (bt) grain from western Maine (WM) showing little to no separation of cleavage associated with the kinks. In a), the kinked mica is an exceptional example of cleavage separation; however, it is still observed at higher frequency in the SCSZ compared to WM. All the kinked micas in a) and b) have their cleavage (black lines) perpendicular to the images.

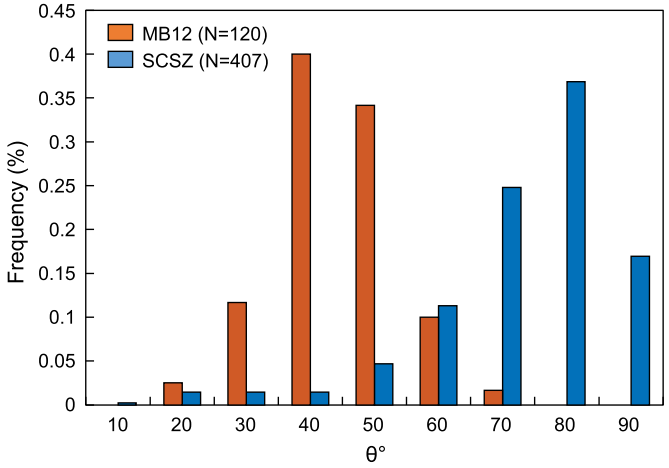

Fig. 10. Histogram of the angle (θ) between the shear plane (mylonitic foliation) and the kink-band boundary. The Misra and Burg (2012; marked by MB12) histogram (orange) indicates the torsion experiments of muscovite aggregates for shear strain of 5.0, and the blue histogram shows the data from the Sandhill Corner shear zone (SCSZ). Total number of measurements (N) is also displayed. Kinks from MB12 exhibit a relatively normal distribution and an average value of 39.3°, whereas those from the SCSZ with a minimum shear strain of ~14.2–30 are negatively-skewed and show a higher average of 69.0°.

stresses accompanying seismicity). These data suggest that mica kink-band geometry can be used to distinguish between dynamic and quasi-static loading histories, and our data from the SCSZ suggest that kink-band geometry could be added to the growing list of indicators of seismic activity in faults/shear zones (e.g., Rowe and Griffith, 2015).

Asymmetric kink bands have been shown to form in torsion experiments in contrast to symmetric kink bands that form during axial compression (Misra and Burg, 2012), so the question arises as to whether the differences between the SCSZ and WM micas reflect different kinematics. Two aspects of the MB12 dataset argue against this possibility. First, the maximum asymmetry from MB12 is ~24° whereas that from the SCSZ is 56°. Second, MB12 demonstrated that histograms of the angle between the kink-band boundary and the shear plane (θ) decreased asymptotically and changed their distribution with increasing shear strain. For example, the average θ of 63.1° for shear strain of 0.2 exhibits a negatively skewed distribution. With increasing shear strain, the distribution becomes approximately normally distributed as θ decreases to 39.3° for shear strain of 5.0 (Misra and Burg, 2012). In contrast, kinks from the SCSZ exhibit a higher average θ of 69.0° and are negatively skewed (Fig. 10). The difference in maximum asymmetry and θ suggests that the kinks from the SCSZ cannot be explained by quasi-static deformation in a simple shear kinematic reference frame. The possibility of the kinks in the SCSZ exhibiting the higher average θ and a negatively skewed distribution due to lower bulk shear strain can be discounted based on: (a) the intense mylonitization and grain-size reduction, and (b) estimated minimum shear strains of ~14.2 from thinned quartz veins (Anderson and Johnson, 2017) and ~30 from sheared veins and surface-area reconstructions of boudin strings (Swanson, 1994).

Rocks deformed at the FVT are subject to quasi-static, interseismic strain rates punctuated by dynamic coseismic loading and rapidly decelerating postseismic strain rates. This complex deformation history has the potential to impact the geometric features of kink bands by episodic overprinting events. While post and interseismic deformation has the potential to influence the geometric features of kink bands along the SCSZ, Johnson et al. (2009) showed that mica fish orientations in the SCSZ indicate a strong viscous decoupling from the surrounding matrix during shearing. Such decoupling would minimize the extent of internal deformation in the mica grains, reducing the probability of forming kinks during viscous flow of the surrounding matrix. Another indication of minimal internal deformation caused by viscous creep is the paucity of secondary and second-generation kink bands (in the sense of E73) in micas from the SCSZ. In contrast, secondary and second-generation kink bands are observed in micas from WM and quasi-static deformation experiments.

Kink-band data from the SCSZ also provide insight on the magnitude of transient, dynamic stresses in the earthquake source region. Because the rocks in the SCSZ appear to have undergone pul-

verization associated with high dynamic strain rates in the vicinity of a propagating rupture (B.R. Song et al., 2020), we can place estimates on the magnitude of these transient dynamic stresses by comparing experimental observations of peak stresses during simulation of dynamic fracturing and pulverization. Split Hopkinson pressure bar experiments on Westerly granite show an increase in the peak compressive strength/dynamic stress with increasing confining pressure (e.g., Yuan et al., 2011). Extrapolation of the experimental results (using a power-law fit with $R^2 = 0.9223$ in Fig. 8 of Yuan et al., 2011) to depths corresponding to the base of the seismogenic zone (i.e., 15–20 km) yields transient dynamic stresses in the range of 1.7–2 GPa required for pulverization. The shock impact experiments of HA69 found that kink banding in lepidomelane occurred in the pressure range of 0.9–3.4 GPa, comparing well with this extrapolation. In addition, Barber and Griffith (2017) showed using the split Hopkinson pressure bar that Arkansas Novaculite required dynamic compressive stresses of ∼1.6 GPa for pulverization in weakly confined experiments, demonstrating the important role of microstructure and grain size in stresses required for pulverization. Therefore, it appears that the SCSZ kink bands may have sustained transient local dynamic stresses of order 1 GPa, although more experimental and field-based work is needed to test this possibility. While these stresses may seem unlikely in relation to the orders of magnitude lower stress drops typically associated with earthquakes (i.e., 0.1–100 MPa; e.g., Cocco et al., 2016 and references therein), recent work by Campbell et al. (2020) shows that GPa-level stress drops can occur in the dry lower crust. We emphasize that elevated stresses on the order of GPa are transient local features facilitated by propagating ruptures and do not reflect the spatially averaged stress drops over entire slip surfaces.

5.4. Applications in determining seismic energy budgets

The proposed evidence suggesting that the kink bands in the SCSZ were formed from dynamic loading associated with earthquakes places these microstructures within a framework applicable to seismic energy budgets. During an earthquake, stored elastic energy is released and partitioned into radiated body waves, frictional heat, and a variety of inelastic processes such as microcracking (Beeler et al., 2012). Of these three contributions, the radiated energy is the only variable that can be directly measured from seismometers and is thought to be a very small fraction of the overall energy budget, roughly less than 15–20% (Lockner and Okubo, 1983; Kanamori et al., 1998; McGarr, 1999). To further constrain the partitioning of the remaining energy into frictional heat and other inelastic dissipative processes, analysis of rocks from the source regions of earthquakes is required.

Typical estimates of the energy associated with frictional heat at the lower reaches of the seismogenic zone come from studies of pseudotachylyte (e.g., Di Toro et al., 2005; Pittarello et al., 2008), whereas particle size distribution analyses of fragmented minerals provide estimates of surface energy (e.g., Chester et al., 2005; B.R. Song et al., 2020). Nanoindentation experiments on micas have revealed that the formation of kink bands can dissipate significant energy due to the hysteretic, nonlinear elastic response during loading and unloading (Basu et al., 2009). Basu et al. (2009) suggests that for a 3 GPa load, this dissipated energy can be on the order of 80 MJ/m^3 per cycle of loading/unloading. Such high-pressure loads, which may have occurred transiently in the SCSZ, are thus expected to contribute to the energy budget of earthquakes in the form of dissipated heat. Such signatures may be detectable within muscovite porphyroclasts via thermometric techniques. Further experimental work utilizing dynamic stress loading on mica aggregates may be helpful in exploring the energetics of kink-band formation during dynamic loading.

6. Conclusions

This study demonstrates that geometric features of kinked micas have the potential to be used as an indicator of paleoseismicity and dynamic loading. Through measurements and a statistical approach, we show that the degree of asymmetry, kink-band width, and angle of external rotation define trends that may be used to distinguish between dynamic and quasi-static loading. Kink bands in micas from the SCSZ show trends consistent with dynamic loading, including higher degrees of kink-band asymmetry, smaller kink-band widths, and greater ranges of external rotation compared to rocks exposed to regional deformation and metamorphism. Our results suggest that micas in the SCSZ experienced GPa-level local, transient stresses associated with rapid dynamic strain rates presumably during propagation of one or more earthquake ruptures.

CRediT authorship contribution statement

Erik K. Anderson: Conceptualization, Formal analysis, Investigation, Validation, Writing – original draft. **Won Joon Song:** Data curation, Formal analysis, Writing – review & editing. **Scott E. Johnson:** Formal analysis, Funding acquisition, Investigation, Resources, Supervision, Writing – review & editing. **Alicia M. Cruz-Uribe:** Formal analysis, Supervision, Writing – review & editing.

Declaration of competing interest

The authors declare that they have no known competing financial interests or personal relationships that could have appeared to influence the work reported in this paper.

Acknowledgements

We acknowledge support from National Science Foundation grant EAR-1727090. We are grateful to Andreas Kronenberg and Anonymous for constructive reviews that led to important improvements to the manuscript.

Appendix A. Supplementary material

Supplementary material related to this article can be found online at https://doi.org/10.1016/j.epsl.2021.117000.

References

Aaron, H.B., Bolling, G.F., 1972. Free volume as a criterion for grain boundary models. Surf. Sci. 31, 27–49. https://doi.org/10.1016/0039-6028(72)90252-X.

Anderson, E., Johnson, S.E., 2017. Minimum finite shear strain estimates and implications for strain localization at the base of the seismogenic zone: a case study from the Sandhill Corner shear zone, Maine, USA. Geological Society of America Abstracts with Programs, Vol. 49, Paper No. 43-1.

Barber, T., Griffith, W.A., 2017. Experimental constraints on dynamic fragmentation as a dissipative process during seismic slip. Philos. Trans. R. Soc. A, Math. Phys. Eng. Sci. 375. https://doi.org/10.1098/rsta.2016.0002.

Baronnet, A., Olives, J., 1983. The geometry of micas around kink band boundaries I. A crystallographic model. Tectonophysics 91, 359–373. https://doi.org/10.1016/0040-1951(83)90050-1.

Basu, S., Zhou, A., Barsoum, M.W., 2009. On spherical nanoindentations, kinking nonlinear elasticity of mica single crystals and their geological implications. J. Struct. Geol. 31, 791–801. https://doi.org/10.1016/j.jsg.2009.05.008.

Beeler, N., Kilgore, B., McGarr, A., Fletcher, J., Evans, J., Baker, S.R., 2012. Observed source parameters for dynamic rupture with non-uniform initial stress and relatively high fracture energy. J. Struct. Geol. 38, 77–89. https://doi.org/10.1016/j.jsg.2011.11.013.

Borg, I., Handin, J., 1966. Experimental deformation of crystalline rocks. Tectonophysics 3, 249–367. https://doi.org/10.1016/0040-1951(66)90019-9.

Bradley, D.C., Tucker, R.D., Lux, D.R., Harris, A.G., McGregor, D.C., 2000. Migration of the Acadian Orogen and Foreland basin across the Northern Appalachians of Maine and adjacent areas. U.S. Geological Survey, Professional Paper 1624. https://pubs.usgs.gov/pp/pp1624/.

Chester, J.S., Chester, F.M., Kronenberg, A.K., 2005. Fracture surface energy of the Punchbowl fault, San Andreas system. Nature 437, 133–136. https://doi.org/10.1038/nature03942.

Campbell, L.R., Menegon, L., Fagereng, Å., Pennacchioni, G., 2020. Earthquake nucleation in the lower crust by local stress amplification. Nat. Commun. 11, 1–9. https://doi.org/10.1038/s41467-020-15150-x.

Cocco, M., Tinti, E., Cirella, A., 2016. On the scale dependence of earthquake stress drop. J. Seismol. 20, 1151–1170. https://doi.org/10.1007/s10950-016-9594-4.

Cowan, D.S., 1999. Do faults preserve a record of seismic slip? A field geologist's opinion. J. Struct. Geol. 21, 995–1001. https://doi.org/10.1016/S0191-8141(99)00046-2.

Dewey, J.F., 1965. Nature and origin of kink-bands. Tectonophysics 1, 459–494. https://doi.org/10.1016/0040-1951(65)90019-3.

Di Toro, G., Pennacchioni, G., Teza, G., 2005. Can pseudotachylytes be used to infer earthquake source parameters? An example of limitations in the study of exhumed faults. Tectonophysics 402, 3–20. https://doi.org/10.1016/j.tecto.2004.10.014.

Etheridge, M.A., Hobbs, B.E., Paterson, M.S., 1973. Experimental deformation of single crystals of biotite. Contrib. Mineral. Petrol. 38, 21–36. https://doi.org/10.1007/BF00371724.

Gerbi, C., West, D.P., 2007. Use of U-Pb geochronology to identify successive, spatially overlapping tectonic episodes during Silurian-Devonian orogenesis in South-central Maine, USA. Bull. Geol. Soc. Am. 119, 1218–1231. https://doi.org/10.1130/B26162.1.

Goodwin, L.B., Wenk, H.R., 1990. Intracrystalline folding and cataclasis in biotite of the Santa Rosa mylonite zone: HVEM and TEM observations. Tectonophysics 172, 201–214. https://doi.org/10.1016/0040-1951(90)90030-C.

Grover, T.W., Fernandes, L.C., 2003. Bedrock geology of the Weeks Mills quadrangle, Maine. Maine Geological Survey, Open-File Map 03-49, color map, scale 1:24,000. http://digitalmaine.com/mgs_maps/31.

Hörz, F., 1970. Static and dynamic origin of kink bands in micas. J. Geophys. Res. 75, 965–977. https://doi.org/10.1029/jb075i005p00965.

Hörz, F., Ahrens, T.J., 1969. Deformation of experimentally shocked biotite. Am. J. Sci. 267, 1213–1229. https://doi.org/10.2475/ajs.267.10.1213.

Johnson, S.E., Dupee, M.E., Guidotti, C.V., 2006. Porphyroblast rotation during crenulation cleavage development: an example from the aureole of the Mooselookmeguntic pluton, Maine, USA. J. Metamorph. Geol. 24, 55–73. https://doi.org/10.1111/j.1525-1314.2005.00621.x.

Johnson, S.E., Jin, Z.H., Naus-Thijssen, F.M.J., Koons, P.O., 2011. Coupled deformation and metamorphism in the roof of a tabular midcrustal igneous complex. Geol. Soc. Am. Bull. 123, 1016–1032. https://doi.org/10.1130/B30269.1.

Johnson, S.E., Lenferink, H.J., Price, N.A., Marsh, J.H., Koons, P.O., West, D.P., Beane, R., 2009. Clast-based kinematic vorticity gauges: the effects of slip at matrix/clast interfaces. J. Struct. Geol. 31, 1322–1339. https://doi.org/10.1016/j.jsg.2009.07.008.

Kanamori, H., Anderson, D.L., Heaton, T.H., 1998. Frictional melting during the rupture of the 1994 Bolivian earthquake. Science 279, 839–842. https://doi.org/10.1126/science.279.5352.839.

Lockner, D.A., Okubo, P.G., 1983. Measurements of frictional heating in granite. J. Geophys. Res. 88, 4313–4320. https://doi.org/10.1029/JB088iB05p04313.

Ludman, A., West, D.P., 1999. Norumbega Fault System of the Northern Appalachians. Geological Society of America, Special Papers 331.

McGarr, A., 1999. On relating apparent stress to the stress causing earthquake fault slip. J. Geophys. Res. 104, 3003–3011. https://doi.org/10.1029/1998JB900083.

Misra, S., Burg, J.-P., 2012. Mechanics of kink-bands during torsion deformation of muscovite aggregate. Tectonophysics 548–549, 22–33. https://doi.org/10.1016/j.tecto.2012.04.014.

Moench, R.H., 1970. Premetamorphic down-to-basin faulting, folding, and tectonic dewatering, Rangeley area, Western Maine. Geol. Soc. Am. Bull. 81, 1463–1496. https://doi.org/10.1130/0016-7606(1970)81[1463:PDFFAT]2.0.CO;2.

Patterson, M.S., Weiss, L.E., 1966. Experimental deformation and folding in phyllite. Geol. Soc. Am. Bull. 77, 343–374. https://doi.org/10.1130/0016-7606(1966)77[343:EDAFIP]2.0.CO;2.

Pittarello, L., Di Toro, G., Bizzarri, A., Pennacchioni, G., Hadizadeh, J., Cocco, M., 2008. Energy partitioning during seismic slip in pseudotachylyte-bearing faults (Gole Larghe Fault, Adamello, Italy). Earth Planet. Sci. Lett. 269, 131–139. https://doi.org/10.1016/j.epsl.2008.01.052.

Price, N.A., Johnson, S.E., Gerbi, C.C., West, D.P., 2012. Identifying deformed pseudotachylyte and its influence on the strength and evolution of a crustal shear zone at the base of the seismogenic zone. Tectonophysics 518–521, 63–83. https://doi.org/10.1016/j.tecto.2011.11.011.

Price, N.A., Johnson, S.E., Gerbi, C.C., Beane, R.J., West, D.P., 2016. Recrystallization fabrics of sheared quartz veins with a strong pre-existing crystallographic preferred orientation from a seismogenic shear zone. Tectonophysics 682, 214–236. https://doi.org/10.1016/j.tecto.2016.05.030.

Ramsay, J.G., 1967. Folding and Fracturing of Rocks. McGraw-Hill Book Company.

Ramsay, J.G., 1962. The geometry of conjugate fold systems. Geol. Mag. 99, 516–526. https://doi.org/10.1017/S0016756800059823.

Rowe, C.D., Griffith, W.A., 2015. Do faults preserve a record of seismic slip: a second opinion. J. Struct. Geol. 78, 1–26. https://doi.org/10.1016/j.jsg.2015.06.006.

Short, N.M., 1966. Effects of shock pressures from a nuclear explosion on mechanical and optical properties of granodiorite. J. Geophys. Res. 71, 1195–1215. https://doi.org/10.1029/jz071i004p01195.

Short, N.M., 1965. A comparison of features characteristic of nuclear explosion craters and astroblemes. Ann. N.Y. Acad. Sci. 123, 573–616. https://doi.org/10.1111/j.1749-6632.1965.tb20389.x.

Smith, H.A., Barreiro, B., 1990. Monazite U-Pb dating of staurolite grade metamorphism in pelitic schists. Contrib. Mineral. Petrol. 105, 602–615. https://doi.org/10.1007/BF00302498.

Song, B.R., Johnson, S.E., Song, W.J., Gerbi, C.C., Yates, M.G., 2020. Coseismic damage runs deep in continental strike-slip faults. Earth Planet. Sci. Lett. 539, 116226. https://doi.org/10.1016/j.epsl.2020.116226.

Song, W.J., Johnson, S.E., Gerbi, C.C., 2020. Quartz fluid inclusion abundance and off-fault damage in a deeply exhumed, strike-slip, seismogenic fault. J. Struct. Geol. 139, 104118. https://doi.org/10.1016/j.jsg.2020.104118.

Stöffler, D., 1966. Zones of impact metamorphism in the crystalline rocks of the Nordlinger Ries Crater. Contrib. Mineral. Petrol. 12, 15–24. https://doi.org/10.1007/BF02651126.

Swanson, M.T., 1994. Late Acadian-Alleghenian transpressional deformation: evidence from asymmetric boudinage in the Casco Bay Area, coastal Maine. J. Struct. Geol. 14, 323–341. https://doi.org/10.1016/0191-8141(92)90090-J.

Twiss, R.J., Moores, E.M., 1992. Structural Geology. W. H. Freeman and Company, New York.

Weiss, L.E., 1980. Nucleation and growth of kink bands. Tectonophysics 65, 1–38. https://doi.org/10.1016/0040-1951(80)90221-8.

West, D.P., Beal, H.M., Grover, T.W., 2003. Silurian deformation and metamorphism of Ordovician arc rocks of the Casco Bay Group, South-central Maine. Can. J. Earth Sci. 40, 887–905. https://doi.org/10.1139/e03-021.

West, D.P., Hubbard, M.S., 1997. Progressive localization of deformation during exhumation of a major strike-slip shear zone: Norumbega fault zone, South-central Maine, USA. Tectonophysics 273, 185–201. https://doi.org/10.1016/S0040-1951(96)00306-X.

West Jr., D.P., Peterman, E.M., 2004. Bedrock geology of the Razorville quadrangle, Maine. Maine geological survey, Open-File Map 04-29, color map, scale 1:24,000. https://digitalmaine.com/mgs_maps/40/.

Yuan, F., Prakash, V., Tullis, T., 2011. Origin of pulverized rocks during earthquake fault rupture. J. Geophys. Res. 116, B06309. https://doi.org/10.1029/2010JB007721.